

# Thermodynamic framework elucidating supersaturation throughout nanocrystal growth

Paul Z. Chen<sup>1</sup>, Aaron J. Clasky<sup>1</sup>, and Frank X. Gu<sup>1,2,\*</sup>

<sup>1</sup>Department of Chemical Engineering and Applied Chemistry, University of Toronto, Toronto, Ontario M5S 3E5, Canada

<sup>2</sup>Institute of Biomedical Engineering, University of Toronto, Toronto, Ontario M5S 3G9, Canada

Supersaturation is the fundamental thermodynamic parameter driving crystal nucleation and growth, yet no method can characterize it during the formation of colloidal nanocrystals (NCs). Here, we develop a framework to experimentally characterize time-resolved profiles of supersaturation throughout NC growth. As demonstrated with Au nanocubes, our methodology can predict the growth profiles of NCs and reveal supersaturation-associated shape evolutions. By altering supersaturation dynamics, we modulate these shape evolutions and NC features with atomic precision. This work paves the way for deeper understanding of the complex phenomena directing nanoscale crystal growth and provides insight for the rational design of NCs.

Nanocrystals (NCs) present structure-dependent properties that can be superior, or unavailable, to bulk crystals [1-6]. Using the mechanistic insight gained by elucidating reaction pathways, synthesis methods can grow NCs with precise size, shape, elemental composition and lattice strain [7-14], facilitating next-generation technologies in heterogenous catalysis, chemical processing, electronics, photonics, energy harvesting, chemical and biological sensing, medicine and environmental remediation [1-6,15-17]. Nonetheless, despite significant interest, the growth of colloidal NCs remains poorly understood, based in part on limited insight into the thermodynamic processes governing growth [18,19].

Supersaturation is the fundamental thermodynamic parameter that drives crystal growth and can be defined by

$$\sigma = \ln \frac{C}{C_\infty} = \frac{\Delta\mu}{k_B T}, \quad (1)$$

where  $C$  is the bulk monomer concentration,  $C_\infty$  is the bulk saturation concentration,  $\Delta\mu$  is the chemical potential and  $k_B T$  is the thermodynamic temperature. To form NCs, synthesis formulations modulate  $C$  above the saturation (enabling growth if nuclei are present) or nucleation limits. For substrate-bound NCs, mechanistic experiments use open reactions and introduce vapor or liquid sources with fixed supersaturations to uncover insight into growth [20-23]. In contrast, colloidal NC syntheses typically use closed conditions, and reactions dynamically convert precursor to monomer throughout crystal formation [Fig. 1(a)]. These processes are complex, and supersaturation profiles during growth have yet to be quantitatively determined, hindering the theoretical modeling as well as mechanistic investigation of colloidal NC growth. Since 1950, the LaMer-Dinegar model, as shown in Fig. 1(b), has guided qualitative understanding of how monomer tends to progress during the nucleation and growth of colloidal NCs [24].

In this Letter, we develop a framework to characterize supersaturation throughout the synthesis of colloidal NCs, enabling theoretical modeling of, and mechanistic insight into, their growth. The methodology uses inputs from facile,

real-time optical techniques to determine time-resolved supersaturation profiles. To show this, we synthesize colloidal Au nanocubes; use the framework to characterize supersaturation throughout growth; predict their growth profile; and show how supersaturation mediates, and can modulate, the features and shape evolutions of NCs during growth.

To develop the framework, we first consider the mass balance for monomer concentration in closed conditions at time  $i$ :  $C_i = C_{i-1} + C_i^{\text{conv}} - C_i^{\text{NC}}$  [Fig. 1(a)]. For  $\Delta t_i \rightarrow 0$ , the supply and consumption concentrations of monomer can be determined by  $C_i^{+/-} = R_i \Delta t_i$ , where  $R_i$  is the intensive form of the molar rate of conversion from precursor to monomer (for  $C_i^{\text{conv}}$ ) or intensive form of the molar rate of monomer consumption due to NC growth (for  $C_i^{\text{NC}}$ ). Colloidal NC syntheses typically involve precursor-limited reactions, which consume monomer as it is produced ( $C_i \approx C_{i-1} \approx 0$ ) [13,25]. Hence, conversion of precursor to monomer coincides with colloidal NC growth and  $R_{\text{conv}}(t) = R_{\text{NC}}(t)$ .

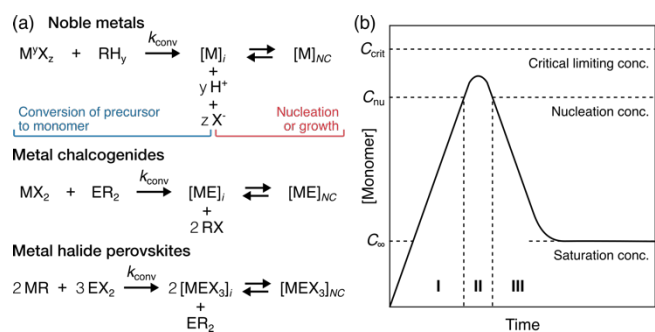


FIG. 1. Precursor-limited nucleation and growth of colloidal NCs. (a) The general reaction pathway of metal precursors for conversion to monomers and NC formation for noble metals, metal chalcogenides or metal halide perovskites. M = metal, X = counterion, R = reactant, y = oxidation state. The reduction pathway of metal halide perovskites was represented by the oleate injection method for ternary NCs. (b) LaMer-Dinegar plot of monomer concentration, in which supersaturation (I) precedes homogenous nucleation (II) and growth (III).

To determine  $\mathbf{R}_{NC}(t)$ , we consider the thermodynamic influences on nanoscale crystallization. The local saturation concentration at the surface of a spherical NC of radius  $r$  is described by the Gibbs-Thomson equation,

$$C(r) = C_\infty \exp\left(\frac{2v_c\gamma}{rRT}\right) \approx C_\infty \left(1 + \frac{2v_c\gamma}{rRT}\right), \quad (2)$$

where  $v_c$  is the molar volume of the monomer,  $\gamma$  is the surface energy and  $R$  is the gas constant [26]. Based on this equation, as obtained by Sugimoto [27] and expanded by Talapin *et al.* [28], the radial growth rate of a single colloidal NC is described by

$$\frac{dr}{dt} = v_c DC_\infty \left[ \frac{\exp(\sigma) - \exp\left(\frac{2v_c\gamma}{rRT}\right)}{r + \frac{D}{k_0^g} \exp\left(\alpha \frac{2v_c\gamma}{rRT}\right)} \right], \quad (3)$$

where  $D$  is the bulk monomer diffusion coefficient,  $\alpha$  is the reaction transfer constant and  $k_0^g$  is the rate constant for bulk growth. As  $2v_c\gamma/RT$  is on the order of nanometers, in the diffusion regime ( $D \ll k_0^g$ ), Eq. (3) simplifies to

$$\frac{dr}{dt} = \frac{v_c DC_\infty}{r} \left[ \exp(\sigma) - \exp\left(\frac{2v_c\gamma}{rRT}\right) \right], \quad (4)$$

Monomer deposits onto surfaces during classical crystal growth, and the areal number of monomer units for a NC is  $A = 4\pi r^2/a^2$ , where  $a$  is the lattice parameter. In turn, the areal growth rate of a single colloidal NC is

$$\frac{dA}{dt} = \frac{dA}{dr} \frac{dr}{dt} = \frac{8\pi v_c DC_\infty}{a^2} \left[ \exp(\sigma) - \exp\left(\frac{2v_c\gamma}{rRT}\right) \right]. \quad (5)$$

As crystal formation coincides with monomer consumption, we use this equation to derive the intensive form of the molar rate of monomer consumption:

$$\mathbf{R}_{NC}(t) = \frac{8\pi v_c n_{NC} DC_\infty}{a^2 N_A V_s} \left[ \exp(\sigma) - \exp\left(\frac{2v_c\gamma}{rRT}\right) \right], \quad (6)$$

where  $n_{NC}$  is the number of NCs undergoing growth,  $N_A$  is Avogadro's number and  $V_s$  is the volume of the synthesis formulation. Thus, the rate of monomer consumption depends on bulk supersaturation and is modulated by the Gibbs-Thomson effect based on the distribution of NC size.

To characterize supersaturation, we use the observation that colloidal NCs show size-dependent optical properties, such as light scattering, extinction and fluorescence [13,29-32]. That is, rather than directly quantify  $\mathbf{R}_{conv}(t)$ , which is experimentally complex, we can use facile, real-time optical techniques to determine  $\mathbf{R}_{NC}(t)$ .

When syntheses directly introduce monomer or quantitatively convert precursor to monomer before seed addition, reactions typically follow pseudo-first-order kinetics [32-35]. Assuming that growth is run to completion, in which the final monomer concentration becomes  $C_\infty$ , the bulk monomer concentration can be described by

$$C_i(t) = (C_0 - C_\infty) \exp(-kt) + C_\infty, \quad (7)$$

where  $k$  is the rate constant and  $C_0$  is the total monomer concentration. The concentration of crystallized monomer is then

$$C_{NC}(t) = (C_0 - C_\infty) - (C_0 - C_\infty) \exp(-kt), \quad (8)$$

and

$$\mathbf{R}_{NC}(t) = -\frac{dC_i}{dt} = k(C_0 - C_\infty) \exp(-kt). \quad (9)$$

When these reactions have an induction period in the conversion from precursor to monomer, the reaction can be described by sigmoidal kinetics:

$$\mathbf{R}_{NC}(t) = -\frac{dC_i}{dt} = \frac{k(C_0 - C_\infty) \exp[k(t-t_0)]}{\{1 + \exp[k(t-t_0)]\}^2}, \quad (10)$$

where  $t_0$  denotes the inflection point, and

$$C_{NC}(t) = (C_0 - C_\infty) - \frac{C_0 - C_\infty}{1 + \exp[k(t-t_0)]}, \quad (11)$$

Re-arranging Eq. (6), we find

$$\sigma(t) = \ln \left[ \frac{a^2 N_A V_s}{8\pi v_c n_{NC} DC_\infty} \mathbf{R}_{NC}(t) + \exp\left(\frac{2v_c\gamma}{rRT}\right) \right], \quad (12)$$

where  $r$  is implicit to the function and  $\mathbf{R}_{NC}(t)$  is specified by Eq. (9) for pseudo-first-order reactions; Eq. (10) for reactions with an induction period; or higher-order equations for reactions with greater kinetic complexity [32,36]. Based on  $2v_c\gamma/RT$ ,  $r > 10$  nm tends to lead to a small contribution from the Gibbs-Thomson effect, and NCs grow at rates comparable to bulk crystals. Supersaturation then becomes an explicit relationship and is described by

$$\sigma(t) = \ln \left[ \frac{a^2 N_A V_s}{8\pi v_c n_{NC} DC_\infty} \mathbf{R}_{NC}(t) + 1 \right]. \quad (13)$$

According to these equations, reactions with lower-order kinetics result in four optically observable profiles of bulk monomer progression (Fig. 2), which each resemble sections of the LaMer-Dinegar plot [Fig. 1(b)].

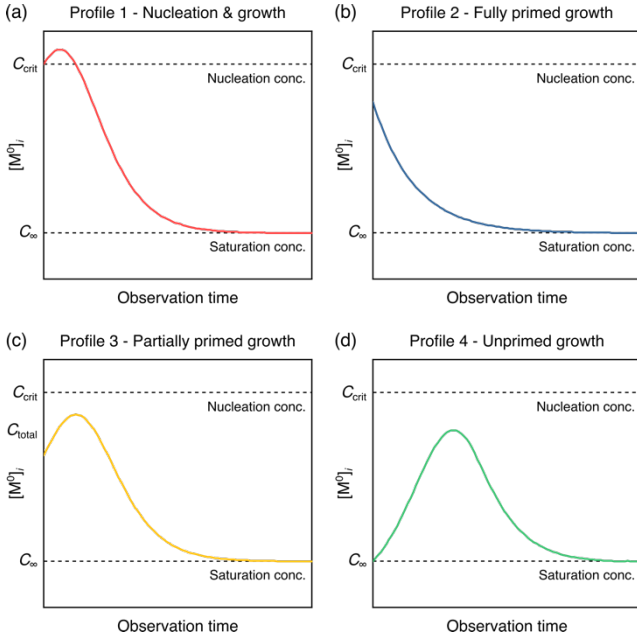


FIG. 2. Observable profiles of bulk monomer during the precursor-limited nucleation or growth of colloidal NCs. Low-order monomer profiles were based on Eqs. (13) and (9) or (10) (a) during homogenous nucleation, (b) after addition of seed to a growth formulation in which precursor has been fully converted to monomer, (c) after addition of seed to a growth formulation in which precursor has been partially converted to monomer and (d) in which conversion of precursor to monomer is initiated by seed addition.

Thus far, we have assumed that NCs undergo layer-by-layer (LBL) growth, a classical mode of crystal growth. While NCs can grow nonclassically by attachment [37-39], they predominantly grow by the classical modes: LBL, normal (N) or dislocation-driven (DD) growth [20-23,27,28,40-42]. Each classical growth mode can be described by its relationship with supersaturation [26]. That is, as we derived in the Supplemental Material, Note 2, growth kinetics can be linked directly to supersaturation, a thermodynamic parameter, through a linear free energy relationship (LFER):

$$\log(k/k_0) = \delta\rho\varepsilon, \quad (14)$$

where  $\delta$  describes the difference in chemical environments between reaction series,  $\rho$  represents the supersaturation-independent variables of growth mechanisms and  $\varepsilon$  is the relative supersaturation term defined as

$$\varepsilon = \begin{cases} \sigma - \sigma_0, & \text{LBL} \\ \log(\sigma - \sigma_0), & \text{DD and N,} \end{cases} \quad (15)$$

with  $k_0$  and  $\sigma_0$  as the rate constant and supersaturation, respectively, of a reference reaction. Thus, by solely modulating  $\sigma$  in a reaction series [43], this LFER can distinguish between modes via  $\varepsilon$  or mechanisms based on the same mode via  $\rho$  (e.g., two facets grow LBL [same

mode] but monomer deposition is favored on one facet [the mechanism], resulting in anisotropic growth).

Using our framework, we investigated the growth of colloidal Au nanocubes. To experimentally assess size and shape evolutions, we arrested growth at various times (Methods) and imaged the NCs using high-angle annular darkfield scanning transmission electron microscopy (HAADF-STEM) [Fig. 3(a)]. Cuboctahedra evolved to truncated cubes and then to cubes [Fig. 3(b)]. As shown in scanning electron (SE)-STEM images [Fig. 3(c)], overgrowth occurred on a proportion of cubes, and other shapes including tetrahedra also appeared during synthesis. We analyzed the yields of the NC shapes throughout growth and found that, after evolving from cuboctahedra, the total yield of NCs with cubic shape (truncated cubes, cubes and overgrown cubes) remained consistent (92.9, 92.3, 92.1 and 93.0% at 2.0, 4.0, 7.0 and 15 min) (Table S1), suggesting that overgrowth occurred on already-formed cubic NCs, rather than during the transition from cuboctahedra to cubes.

Based on growth kinetics measured via extinction [Fig. 3(d)], progression of the full extinction spectra is shown in Fig. S1, we used Eqs. (10) and (13) to characterize the time-resolve supersaturation profile in the colloidal system [Fig. 3(e)], equation parameters shown in Table S2]. Using this supersaturation profile, we modeled colloidal nanocube growth using Eq. (4). Notably, the theoretical growth profile predicted the experimental one [Fig. 3(f)], supporting that supersaturation dynamics were properly interpreted for these NCs. We also characterized supersaturation by imaging the color development during growth, finding agreement between imaging and spectrophotometry and further showing utility of this methodology (Fig. S3). Furthermore, we compared the shape yields throughout growth to the supersaturation profile, which indicated that overgrowth was associated with supersaturation [Fig. 3(e)]. More specifically, overgrowth occurred predominantly when supersaturation was high in the early stages of synthesis.

Based on these cumulative insights, we rationalized that reducing growth kinetics in the early stages of synthesis would mitigate cube overgrowth. As informed by Eqs. (14) and (15), we decreased supersaturation to reduce growth rate. The synthesis formulation for the NCs shown in Fig. 3 used 0.1 molar equivalents (eqv., relative to Au added) of NaOH. Supersaturation was modulated by replacing NaOH with HCl, as  $H^+$  and  $Cl^-$  are chemically endogenous to the synthesis formulation, are labile ions and should decrease the bulk monomer concentration (Fig. S4) [44].

Figure 4(a-c) shows the products of these syntheses, with larger-area micrographs shown in Fig. S5. We characterized the growth kinetics of these formulations via extinction (Fig. S6), which indicated that these additions of HCl reduced supersaturation, particularly in the early stages of synthesis [Fig. 4(d)]. This indeed diminished the proportion of overgrown nanocubes [Fig. 4(e)], shape yields summarized in Table S3]. For 0.1 eqv. NaOH, 17.1% of the NCs were overgrown nanocubes. For 1 eqv. HCl and 2 eqv. HCl, the yield of overgrown nanocubes diminished to 7.5% and 4.0%, respectively. Concomitantly, increasing the amounts of HCl led to the emergence of tetrahedra [Fig. 4(e)].

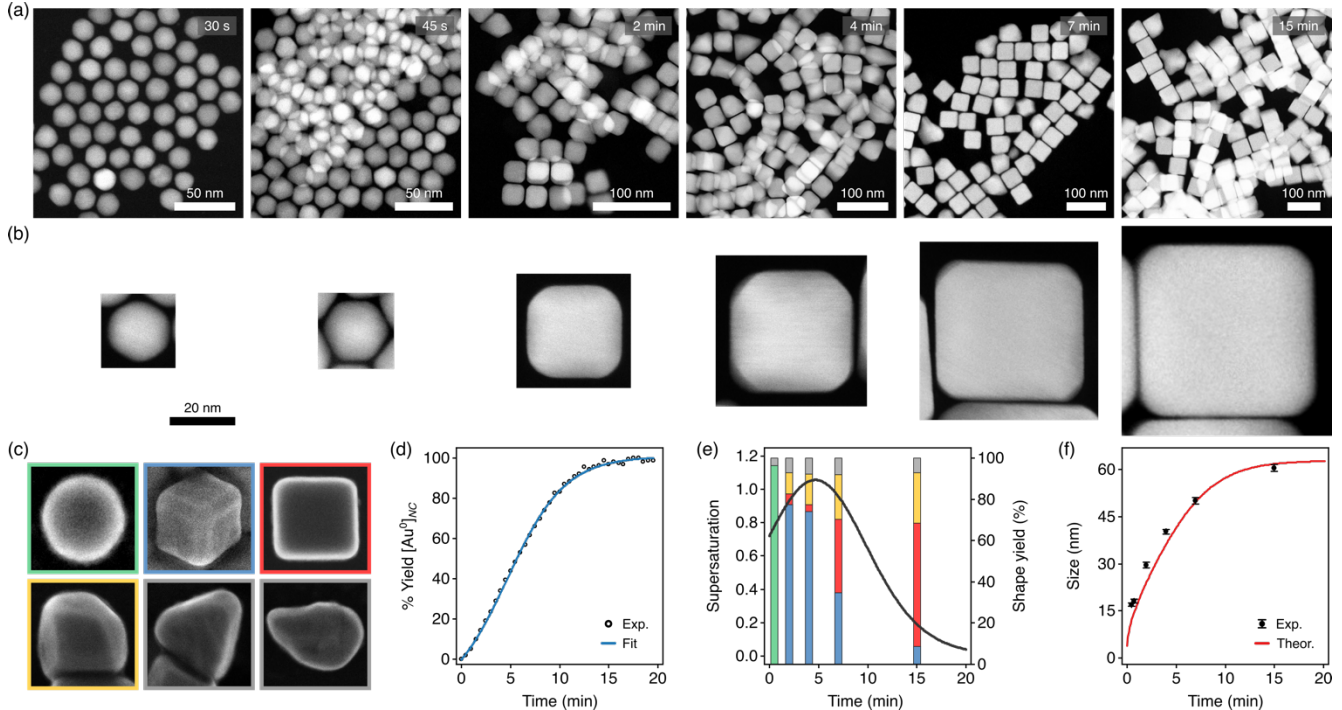


FIG. 3. Supersaturation-dependent growth and shape evolution of Au nanocubes. (a) HAADF-STEM images of the NCs found throughout colloidal nanocube growth. Times denote when growth was arrested. (b) HAADF-STEM images of single NCs from the above samples depicting the transition of cuboctahedra to cubes. The scale bar applies to each micrograph. (c) SE-STEM images of the major NC shapes found throughout colloidal nanocube growth. Cuboctahedra (green), truncated cubes (blue), cubes (red), overgrown cubes (yellow), tetrahedra (grey) and other shapes (grey). (d) Kinetics of NC growth analyzed via peak nanoplasmonic extinction. The data were fitted to Eq. (11) ( $r^2 > 0.99$ ). (e) Time-resolved supersaturation profile (black curve) overlaid on shape yields (bars) at 0.5, 2, 4, 7 and 15 min throughout colloidal nanocube growth. Shapes are denoted by the colors in (c). (f) Experimental and theoretical growth for colloidal nanocubes. Theoretical growth was modelled using the supersaturation profile from (e). Dots and bars represent mean and SD.

The sharpness of nanocube corners decreased as increasing amounts of HCl were added [Fig. 4(d)], which was likely due to the changes in supersaturation [45]. With more HCl, the yield of truncated cubes increased while the yield of cubes decreased [Fig. 4(e)]. For 0.1 equiv. NaOH, 32.6% of the NCs were truncated nanocubes. This proportion increased to 56.7% for 1 equiv. HCl and then 67.9% for 2 equiv. HCl.

We sized the nanocubes to further evaluate the influence of the supersaturation profile on their structural features. The nanocubes had similar overall sizes across the three synthesis formulations (Table S4), and we measured a sharpness index for each NC ( $S$ ), as described in Fig. 4(f). Figure S7 shows measurements by sharpness index, which was normalized by NC size. For 0.1 equiv. NaOH, the mean estimate of  $S$  was 16.3 (95% confidence interval [CI]: 15.9–16.6) nm, whereas it was 15.3 (15.0–15.6) nm for 1 equiv. HCl and 13.3 (12.9–13.7) nm for 2 equiv. HCl. These values were equivalent to 68.9 (67.6–70.2)  $d_{111}$  for 0.1 equiv. NaOH, 65.1 (63.8–66.4)  $d_{111}$  for 1 equiv. HCl and 56.3 (54.6–58.0)  $d_{111}$  for 2 equiv. HCl, where  $d_{111}$  denotes {111} interplanar distances (the corners of face-centered cubic nanocubes point in the <111> direction) [42]. Thus, slight modifications in the supersaturation profile modulated nanocube corners with atomic precision.

In summary, we developed a thermodynamic framework and the accompanying methodology to characterize supersaturation throughout NC synthesis. Remarkably, these quantitative profiles resemble the qualitative ones originally conceptualized by LaMer and Dinegar in 1950 [24]. Based on these profiles, NC growth can be modeled and predicted theoretically, and complex size and shape evolutions can be associated with supersaturation dynamics. These insights potentiate the rational design of colloidal NCs, including with atomic precision.

Since NCs generally interact with light as a size-dependent property, our approaches can be employed to broadly study supersaturation during NC formation. The framework also presents additional opportunities not experimentally explored here. Characterizing monomer concentrations during nucleation may uncover critical nucleation concentrations [Fig. 2(a)]. The LFER in Eqs. (14) and (15) links NC kinetics with bulk thermodynamics, presenting a way to systematically study the mechanisms and modes of NC growth. Moreover, the relevance of these findings also extends beyond nanoscience, materials science and physical chemistry, as better understanding the phenomena that direct nanoscale crystal formation may facilitate the development of key technologies in a broad range of fields, from medicine to energy.

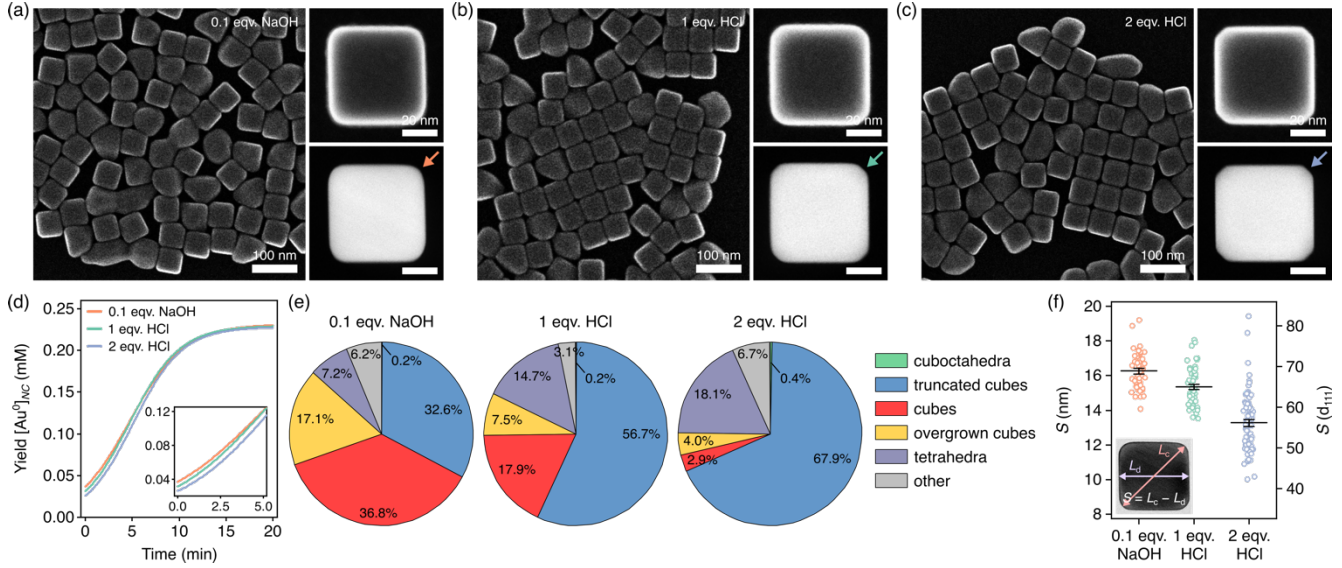


FIG. 4. Supersaturation dynamics mediate shape evolutions during NC growth. (a-c) SE-STEM image of the NCs (left) and SE-STEM (top right) and HAADF-STEM (bottom right) image of an individual nanocube when grown with (a) 0.1 equivalents (equiv.) NaOH, (b) 1 equiv. HCl or (c) 2 equiv. HCl. The arrows point to nanocube corners, which increasingly truncate. (d) Time-resolved conversion kinetics for colloidal nanocube growth. Inset, early kinetics. (e) Shape yields for the various formulations. (f) Comparison of the corner sharpness of nanocubes. Inset, schematic representation of the measurements and sharpness index ( $S$ ).  $S$  is depicted in units of nm and  $\langle 111 \rangle$  interplanar distances. Lines and whiskers represent means and 95% CIs.

This work was funded by the Natural Sciences and Engineering Research Council of Canada (NSERC). P.Z.C. was supported by the NSERC Vanier Scholarship (608544). A.J.C. was supported by the Ontario Graduate Scholarship. F.X.G. was supported by the NSERC Senior Industrial Research Chair and NSERC Discovery Grant.

\*f.gu@utoronto.ca

- [1] A. P. Alivisatos, *Science* **271**, 933 (1996).
- [2] K. T. Shimizu, W. K. Woo, B. R. Fisher, H. J. Eisler, and M. G. Bawendi, *Phys. Rev. Lett.* **89**, 117401 (2002).
- [3] P. D. Howes, R. Chandrawati, and M. M. Stevens, *Science* **346**, 1247390 (2014).
- [4] P. Z. Chen, L. Pollit, L. Jones, and F. X. Gu, *Chem* **4**, 2301 (2018).
- [5] J. Shamsi, A. S. Urban, M. Imran, L. De Trizio, and L. Manna, *Chem. Rev.* **119**, 3296 (2019).
- [6] E. Ozbay, *Science* **311**, 189 (2006).
- [7] Y. Sun and Y. Xia, *Science* **298**, 2176 (2002).
- [8] N. R. Jana, L. Gearheart, and C. J. Murphy, *J. Phys. Chem. B* **105**, 4065 (2001).
- [9] H. Liu and C. Di Valentin, *Phys. Rev. Lett.* **123**, 186101 (2019).
- [10] T. Chookajorn and C. A. Schuh, *Phys. Rev. B* **89**, 064102 (2014).
- [11] P. C. Chen, M. Liu, J. S. Du, B. Meckes, S. Wang, H. Lin, V. P. Dravid, C. Wolverton, and C. A. Mirkin, *Science* **363**, 959 (2019).
- [12] B. C. Steimle, J. L. Fenton, and R. E. Schaak, *Science* **367**, 418 (2020).

- [13] M. P. Hendricks, M. P. Campos, G. T. Cleveland, I. Jen-La Plante, and J. S. Owen, *Science* **348**, 1226 (2015).
- [14] P. B. Green, P. Narayanan, Z. Li, P. Sohn, C. J. Imperiale, and M. W. B. Wilson, *Chem. Mater.* **32**, 4083 (2020).
- [15] W. Lu and C. M. Lieber, *Nat. Mater.* **6**, 841 (2007).
- [16] T. Leshuk, A. B. Holmes, D. Ranatunga, P. Z. Chen, Y. S. Jiang, and F. X. Gu, *Env. Sci. Nano* **5**, 509 (2018).
- [17] A. J. Clasky, J. D. Watchorn, P. Z. Chen, and F. X. Gu, *Acta Biomater.* **122**, 1 (2021).
- [18] M. L. Personick and C. A. Mirkin, *J. Am. Chem. Soc.* **135**, 18238 (2013).
- [19] L. M. Liz-Marzan and M. Grzelczak, *Science* **356**, 1120 (2017).
- [20] S. A. Morin, M. J. Bierman, J. Tong, and S. Jin, *Science* **328**, 476 (2010).
- [21] M. J. Bierman, Y. K. Lau, A. V. Kvit, A. L. Schmitt, and S. Jin, *Science* **320**, 1060 (2008).
- [22] J. Zhu, H. Peng, A. F. Marshall, D. M. Barnett, W. D. Nix, and Y. Cui, *Nat. Nanotechnol.* **3**, 477 (2008).
- [23] J. Joo, B. Y. Chow, M. Prakash, E. S. Boyden, and J. M. Jacobson, *Nat. Mater.* **10**, 596 (2011).
- [24] V. K. Lamer and R. H. Dinegar, *J. Am. Chem. Soc.* **72**, 4847 (1950).
- [25] M. P. Hendricks, B. M. Cossairt, and J. S. Owen, *ACS Nano* **6**, 10054 (2012).
- [26] I. V. Markov, *Crystal growth for beginners: fundamentals of nucleation, crystal growth and epitaxy* (World Scientific, Singapore, 2017), 3rd edn.
- [27] T. Sugimoto, *Adv. Colloid Interface Sci.* **28**, 65 (1987).

- [28] D. V. Talapin, A. L. Rogach, M. Haase, and H. Weller, *J. Phys. Chem. B* **105**, 12278 (2001).
- [29] C. F. Bohren and D. R. Huffman, *Absorption and scattering of light by small particles* (Wiley, New York, 1983).
- [30] S. K. Brar and M. Verma, *Trends Anal. Chem.* **30**, 4 (2011).
- [31] W. Haiss, N. T. Thanh, J. Aveyard, and D. G. Fernig, *Anal. Chem.* **79**, 4215 (2007).
- [32] T. H. Yang, K. D. Gilroy, and Y. Xia, *Chem. Sci.* **8**, 6730 (2017).
- [33] Y. Wang, H. C. Peng, J. Liu, C. Z. Huang, and Y. Xia, *Nano Lett.* **15**, 1445 (2015).
- [34] A. Ruditskiy, M. Zhao, K. D. Gilroy, M. Vara, and Y. N. Xia, *Chem. Mater.* **28**, 8800 (2016).
- [35] M. Zhou *et al.*, *J. Am. Chem. Soc.* **138**, 12263 (2016).
- [36] M. A. Watzky and R. G. Finke, *J. Am. Chem. Soc.* **119**, 10382 (1997).
- [37] R. Takahata, S. Yamazoe, K. Koyasu, K. Imura, and T. Tsukuda, *J. Am. Chem. Soc.* **140**, 6640 (2018).
- [38] P. Guo and Y. Gao, *Phys. Rev. Lett.* **124**, 066101 (2020).
- [39] M. Song, G. Zhou, N. Lu, J. Lee, E. Nakouzi, H. Wang, and D. Li, *Science* **367**, 40 (2020).
- [40] Y. Xia, X. Xia, and H. C. Peng, *J. Am. Chem. Soc.* **137**, 7947 (2015).
- [41] X. Ye *et al.*, *Science* **354**, 874 (2016).
- [42] H. G. Liao, D. Zhrebetskyy, H. Xin, C. Czarnik, P. Ercius, H. Elmlund, M. Pan, L. W. Wang, and H. Zheng, *Science* **345**, 916 (2014).
- [43] N. B. Chapman and J. Shorter, *Advances in linear free energy relationships* (Plenum Press, London, 1972).
- [44] N. Almora-Barrios, G. Novell-Leruth, P. Whiting, L. M. Liz-Marzan, and N. Lopez, *Nano Lett.* **14**, 871 (2014).
- [45] D. Alpay, L. Peng, and L. D. Marks, *J. Phys. Chem. C* **119**, 21018 (2015).

**Supplementary materials for**

**Thermodynamic framework elucidating supersaturation  
throughout nanocrystal growth**

Paul Z. Chen<sup>1</sup>, Aaron J. Clasky<sup>1</sup>, and Frank X. Gu<sup>1,2,\*</sup>

<sup>1</sup>*Department of Chemical Engineering and Applied Chemistry, University of Toronto,  
Toronto, Ontario M5S 3E5, Canada*

<sup>2</sup>*Institute of Biomedical Engineering, University of Toronto, Toronto, Ontario M5S 3G9, Canada*

## I. MATERIALS & METHODS

### Materials

Gold(III) chloride hydrate ( $\text{HAuCl}_4 \cdot x\text{H}_2\text{O}$ ,  $x \approx 3$ ; >99.995%), sodium bromide (NaBr, >99.99%), cetyltrimethylammonium bromide (CTAB, >99%), cetyltrimethylammonium chloride (CTAC, >99%), L-ascorbic acid (>99.0%), sodium borohydride (NaBH<sub>4</sub>, >99.99%), sodium hydroxide (NaOH, >98%), hydrochloric acid (HCl, 37%), thiol-terminated polystyrene (PS-thiol, 5 kDa, polydispersion index ≤1.1), tetrahydrofuran (THF, 99.9%) and toluene (99.8%) were purchased from Sigma-Aldrich (Oakville, ON, Canada). Unless otherwise specified, MilliQ water (18.2 MΩ.cm at 25 °C; Milli-Q® Reference Water Purification System; MilliporeSigma, Oakville, ON, Canada) was used for the experiments. Quartz cuvettes (20 ml) were purchased from Thermo Fisher Scientific (Ottawa, ON, Canada). Scintillation vials (20 ml) were purchased from VWR International (Mississauga, ON, Canada). Reagents were used as received.

### Synthesis of colloidal Au nanocubes

The synthesis procedures were adapted from Park et al. [1].

*Nanoseed preparation.* In a 20 ml scintillation vial, 10 mM HAuCl<sub>4</sub> (250 µl) was added to a solution of 100 mM CTAB (9.75 ml), followed by the rapid addition of ice-cold 10 mM NaBH<sub>4</sub> (600 µl). Samples were stirred at room temperature for 2 min at 1400 rpm and then placed in an incubator at 27°C for 3 h to nucleate nanoseeds. Samples were brown in color, indicating small colloidal NCs. To further grow the nanoseeds, 200 mM CTAC (2 ml), 100 mM ascorbic acid (1.5 ml), the above nanoseed solution (50 µl) and 0.5 mM HAuCl<sub>4</sub> (2 ml) were added sequentially to a 20 ml scintillation vial and stirred at room temperature for 15 min at 300 rpm. The color progressed to red, indicating growth. Samples were then twice centrifuged at 20,600xg for 30 min. The first resuspension was with MilliQ (1 ml) and the second was with 20 mM CTAC (1 ml).

*Nanocube synthesis.* In a 20 ml quartz cuvette, 100 mM CTAC (6 ml); 40 mM NaBr (30 µl); nanoseeds (30 µl); HCl or NaOH (200 µl, see below); 10 mM ascorbic acid (390 µl, dropwise); and 0.5 mM HAuCl<sub>4</sub> (6 ml) were added sequentially and then mixed via pipette. Aside from initial pipette mixing, the solution was left untouched. The concentration of HCl or NaOH added was modified according to the experiment: 0.1 equivalents (eqv.) NaOH (1.5 mM), 1 eqv. HCl (15 mM) or 2 eqv. HCl (30 mM). Molar equivalents refer to the molar ratio with Au added.

### Optical characterization of NC growth

Nanocubes were synthesized in 20 ml quartz cuvettes (path length, 1 cm) as described above. To characterize growth via extinction, the cuvettes were placed in darkness in an apparatus, which passed light from a source (OceanOptics, Orlando, USA) using fiber optic cables

(OceanView Optics, Orlando, USA), 10-m round subminiature assembly (SMA) connectors and detector collection lenses (L4 chamfered; OceanView Optics, Orlando, USA) to an in-line UV/Vis spectrometer (Flame T spectrometer; OceanView Optics, Orlando, USA) with a 4000-series detector (350-1000 nm filter; OceanView Optics, Orlando, USA). Extinction spectra (400-900 nm, step size: 0.217 nm) were collected every 30 s. To characterize growth via nanoplasmonic color, the cuvettes were imaged (EOS Rebel T7i with EF 100 mm macro lens, Canon Canada, Inc., Toronto, ON, Canada) under fume hood lighting every 30 s or 1 min. The addition of HAuCl<sub>4</sub> marked the start time (0 s).

### Arresting colloidal NC growth

The growth of colloidal NCs was arrested via ligand exchange and solvent transfer based on a procedure adapted from Park et al. [2]. Nanocubes were prepared as previously described with 0.1 eqv. NaOH. At various time points, 8 ml of colloidal NCs was quickly added to a THF solution of 1.1 mM PS-thiol (10 ml) in a 20 ml scintillation vial. This solution was vortexed aggressively (>2 min) until it became grey and translucent. This procedure was used for each time point (30 s, 45 s, 2 min, 4 min, 7 min and 15 min).

Samples were left at room temperature overnight to allow the colloidal NCs to settle in the vial. After this, most of the liquid was removed from the vial via pipetting, and vials were placed under reduced pressure until the liquid had evaporated (>2 h). Next, 1 ml toluene was added to each sample, followed by sonication to resuspend the NCs. Samples were then twice centrifuged at 21,000xg for 25 min. The first and second resuspensions were with 1.0 and 0.1 ml of toluene, respectively.

### Scanning transmission electron microscopy

STEM samples were prepared by drop casting the respective solution (5 µl) on a 400-mesh pure C, Cu grid (Ted Pella, Inc., Redding, USA) and dried under hood evaporation. Before drop casting, colloidal NCs were prepared via centrifugation and resuspension in MilliQ. Grids were cleaned via ultraviolet light (5-15 min per side) before imaging. HAADF-STEM and SE-STEM images were acquired using a Hitachi HF-3300 300 kV Environmental TEM with an electron acceleration voltage of 300 kV.

### NC sizing and counting

For sizing, two representative large-area HAADF-STEM images were analyzed using ImageJ (version 1.51s; National Institutes of Health, USA), yielding  $n \geq 40$  NCs for each time point. Each NC that could be clearly delineated in its HAADF-STEM image was sized. For cubes, four measurements were taken for each NC: two corner-to-corner (C) and two edge-to-edge (E) measurements [Fig. S3(a)]. For cuboctahedra, three side-to-side (D) measurements were taken [Fig. S3(b)]. The data were presented as mean for each time point.

To characterize the shape yields at each time point, each NC was assessed for its shape in four representative large-area HAADF-STEM images. For a perfect nanocube,  $C = E\sqrt{2}$  based on the parameters described in Fig. S3, where  $C = \max(C_1, C_2)$  and  $E = \min(E_1, E_2)$ . To delineate truncated cubes from cubes [1], we applied a factor threshold of 1.3; that is, truncated cubes ( $C < 1.3E$ ) were below this threshold, whereas cubes ( $C \geq 1.3E$ ) were equal to or above it. The count for each shape was summed from these images, and yields were presented as percentages of the overall number of NCs counted.

## II. LINEAR FREE ENERGY RELATIONSHIP

We formulated a linear free energy relationship (LFER) to delineate the modes as well as mechanisms of classical crystal growth based on the relationship between supersaturation and growth kinetics. This supplementary note summarizes the three modes of classical crystal growth in the diffusion regime, based on their descriptions in [3], and describes the formulation of a LFER that comprehensively describe classical crystal growth.

### Normal growth

Normal (N) growth occurs above the roughening temperature of a metal. Above this threshold, entropy effects cause crystal surfaces to be atomically rough, presenting an abundance of kink sites in which monomer can directly incorporate. Hence, the rate of normal growth depends on the probability of finding a kink and the monomer flux and, in solution, can be described by

$$R_N = \beta_s v_c (C - C_\infty), \quad (\text{S1})$$

where  $v_c$  is the molar volume of a Au atom in the crystal,  $C$  is the monomer concentration and  $\beta_s$  is the kinetic coefficient for normal crystallization in solution that, in the case of lower supersaturations, is approximated by

$$\beta_s = av \left( \frac{a}{\delta_0} \right)^2 \exp \left( -\frac{\Delta U}{k_B T} \right), \quad (\text{S2})$$

in which  $a$  is the lattice parameter,  $v$  is the vibrational frequency of an adatom,  $(a/\delta_0)^2$  represents the geometric probability that a monomer finds a kink site on the crystal surface from solution,  $\Delta U$  is the kinetic barrier for the incorporation of monomer into a kink site and  $k_B T$  is the thermodynamic temperature. As seen in Eq. (S1), when supersaturation is small ( $\sigma \approx C - C_\infty$ ), it forms a linear relationship with the rate of N growth.

### Dislocation-driven growth

Like N growth, dislocation-driven (DD) and layer-by-layer (LBL) growth occur in the direction normal to the

crystal surface. In these modes, steps are oriented parallel to the crystal facet and spread laterally as monomer incorporates. That is, growth occurs as steps fill laminarly. Hence, the growth rate is based on the rate of step advance  $v$  and the density of steps  $p$ :

$$R = pv. \quad (\text{S3})$$

Dislocations generate steps on a crystal surface, into which monomer incorporates. Screw dislocations, the predominant dislocation driving DD growth, present perpetuating steps with height equal to their Burgers vector. Monomer advances the step, forming a secondary step normal to it but still along the crystal facet. Above the critical edge length for two-dimensional nucleation, monomer incorporates into the secondary step, advancing it and leading to the formation of a tertiary step when it reaches the critical edge length. This process leads to the characteristic spiral growth profile, and DD growth rate can be described in the diffusion regime by

$$R_D = B \frac{\sigma^2}{\sigma_c^2} \left\{ \ln \left[ \left( \frac{d}{\pi a} \right) \frac{\sigma_c}{\sigma} \sinh \left( \frac{\sigma}{\sigma_c} \right) \right] \right\}^{-1}, \quad (\text{S4})$$

where  $\sigma_c$  is the characteristic supersaturation defined by

$$\sigma_c = \frac{19\kappa a^2}{\pi n k_B T d}, \quad (\text{S5})$$

in which  $\kappa$  is the specific step edge energy,  $n$  is the number of dislocations and  $B$  is the rate constant defined by

$$B = \frac{DC_0 v_c}{d}, \quad (\text{S6})$$

where  $D$  is the bulk diffusion coefficient of the monomer and  $d$  is the thickness of the stagnant layer.

The characteristic supersaturation delineates two limiting cases of DD growth with distinct profiles. In the case  $\sigma \ll \sigma_c$ ,  $\sinh(\sigma/\sigma_c) \approx \sigma/\sigma_c$  and Eq. (S4) simplifies to

$$R_{D,1} = \frac{B}{\ln(d/\pi a)} \frac{\sigma^2}{\sigma_c^2}, \quad (\text{S7})$$

which has a parabolic relationship with supersaturation. In the other case ( $\sigma \gg \sigma_c$ ), Eq. (S4) simplifies to

$$R_{D,2} = B\sigma, \quad (\text{S8})$$

which has a linear relationship with supersaturation.

### Layer-by-layer growth

LBL growth involves the formation of two-dimensional nuclei on crystal surfaces to present steps for growth. The mononuclear LBL growth rate is described by

$$R_{LBL} = J_0 Ah \quad (\text{S9})$$

where  $A$  is the surface area of the facet,  $h$  is the step height and  $J_0$  is the rate of two-dimensional nucleation defined by

$$J_0 = vCv_c\sigma^{1/2} \exp\left(-\frac{\Delta U}{k_B T}\right) N_0 \exp\left(-\frac{\pi\chi^2 a^2}{k_B T \Delta \mu}\right), \quad (\text{S10})$$

where  $v$  is the adatom vibrational frequency and  $N_0$  is the adsorption site density.

Polynuclear LBL growth arises when the rate of two-dimensional nucleation exceeds the time taken to complete the lateral growth of a layer, which occurs above the critical facet size determined by

$$L = (v/J_0)^{1/3}. \quad (\text{S11})$$

Above this threshold, the polynuclear LBL growth rate can be described by

$$\begin{aligned} R_{pLBL} &= v_c [\pi a v C (C_0 D d^{-1} y_0)^2 N_0]^{1/3} \sigma^{5/6} \\ &\exp\left(-\frac{\Delta U}{3k_B T}\right) \exp\left(-\frac{\pi\chi^2 a^2}{3k_B T \Delta \mu}\right), \end{aligned} \quad (\text{S12})$$

where  $y_0$  is the interstep distance.

#### *Formulation of the linear free energy relationship*

LFERs are semi-empirical equations that relate logarithmic forms of the thermodynamics and kinetics of reaction series [4]. Supersaturation, a thermodynamic parameter, modulates the rate of crystal growth, a kinetic quantity, and we hypothesized that classical crystal growth could be comprehensively described by a LFER. To formulate it, we first considered the forms of their growth equations, as we derived above. At low supersaturations,  $R_N$  has a linear relationship with  $\sigma$ , that is,  $R_N = \rho_N \sigma$ , where  $\rho$  represents the supersaturation-independent terms. For DD growth,  $R_{D,1}$  has a parabolic relationship with  $\sigma$  ( $R_{D,1} = \rho_{N,1} \sigma^2$ ), whereas  $R_{D,2}$  has a linear relationship with  $\sigma$  ( $R_{D,2} = \rho_{N,2} \sigma$ ). As described in [5],  $R_{LBL}$ , and hence  $R_{pLBL}$ , has an exponential relationship with supersaturation within the range typical for NC growth ( $R_{LBL} = \rho_{LBL} e^\sigma$ ).

To expand this framework, we consider the difference between crystal growth reactions: one reference reaction and one, or more, other reaction(s) with the supersaturation modified. After taking the logarithm of the difference in this reaction series, we formulate, and postulate, our LFER:

$$\log(k/k_0) = \delta\rho\varepsilon, \quad (\text{S13})$$

where  $\delta$  describes the difference in chemical environments between reaction series,  $\rho$  represents the supersaturation-independent parameters that can delineate growth mechanisms, and  $\varepsilon$  is the relative supersaturation term described by

$$\varepsilon = \begin{cases} \frac{\sigma - \sigma_0}{\log(\sigma - \sigma_0)}, & \text{LBL} \\ \log(\sigma - \sigma_0), & \text{DD and N}, \end{cases} \quad (\text{S14})$$

with  $k$  and  $\sigma$  as the rate constant and supersaturation of crystal growth reaction, respectively, and  $k_0$  and  $\sigma_0$  as the parameters from the reference reaction. Note that both limiting cases of DD growth result in  $\varepsilon = \log(\sigma - \sigma_0)$ , based on the application of the logarithm, and these two cases can be differentiated based on  $\rho$ . For mathematical consistency, we typically take  $\delta$  to be negative.

According to Eqs. (S13) and (S14), by solely modulating supersaturation, the modes of classical crystal growth can be distinguished by  $\varepsilon$ , while mechanisms can be additionally differentiated by  $\rho$ . Moreover, the N and DD modes of growth can be distinguished based on the local temperature relative to the roughening temperature [3]. As nanoscale crystal growth often occurs via classical modes, the LFER becomes a powerful tool to investigate how NCs grow, in addition to how macroscopic crystals grow. As this study develops a method to characterize the time-resolved profile of supersaturation throughout colloidal NC growth, the LFER can also be applied to colloidal systems. Moreover, as shown in Fig. 1(a), the general reaction pathways of colloidal NC growth appear similar, suggesting that supersaturation modulation paired with our LFER can be applied to study how many different types of NCs grow.

### III. KINETICS OF NANOCRYSTAL GROWTH VIA NANOPLASMONIC EXTINCTION AND COLOR

We characterized the growth kinetics of the colloidal Au nanocubes via their extinction or colorimetric profiles. As the NC growth had an initial induction period, we used Eq. (10), and the kinetics based on extinction were analyzed by

$$\% \text{ Yield } [\text{Au}^0]_{NC,i} = \frac{E_i - \min(E)}{\max(E) - \min(E)}, \quad (\text{S15})$$

where  $E_i$  represents the peak extinction at time  $i$  and  $\max(E)$  and  $\min(E)$  represent the maximum and minimum peak extinction throughout growth. The extinction spectra were collected using the in-line spectrometer (Methods) and the peak extinction refers to the highest extinction value at the peak wavelength between 500-600 nm. The full spectra along time are shown in Fig. S2.

As the nanoplasmonic color of the colloidal NCs was red (Fig. S4), we used the G value after red-green-blue (RGB) analysis using ImageJ (version 1.51s; National Institutes of Health, USA) to characterize growth kinetics via color. To normalize the intrinsic variation among images in white balance, we used  $G_{N,i} = G_{N,NC} - G_{N,C}$ , where  $G_{N,i}$  represents the normalized G value,  $G_{N,NC}$  represents the G value from the colloidal NC solution and  $G_{N,C}$  represents the G value

from the background for the  $i$ th image. The kinetics of colloidal NC growth were then analyzed by

$$\% \text{ Yield } [\text{Au}^0]_{NC,i} = \frac{\max(\mathbf{G}_N) - G_{N,i}}{\max(\mathbf{G}_N) - \min(\mathbf{G}_N)}, \quad (\text{S16})$$

where  $\max(\mathbf{G}_N)$  and  $\min(\mathbf{G}_N)$  represent the maximum and minimum normalized G values for the array of images, respectively. The color images were collected as described in the Methods.

#### IV. THEORETICAL MODELING OF NANOCRYSTAL GROWTH

We used the thermodynamic framework developed in this study to model the theoretical growth of the colloidal NCs. The time-resolved supersaturation profile for a sample was estimated using Eq. (13), with the equation parameters summarized in Table S2. Eq. (6) was then used to model the growth of the colloidal nanocrystals. Since the molar ratio of NaBr and HAuCl<sub>4</sub> was low in the growth formulation,  $C_\infty$  was estimated based on the equilibrium concentration of [AuCl<sub>2</sub>] [5]. We approximated  $n_{NC}$  assuming spherical nanoseeds with a size of 2.5 nm after the initial nucleation step in nanoseed synthesis. After the secondary growth step in nanoseed synthesis (Methods), the size of the nanoseeds  $d_i$ , which was the initial size of the colloidal NCs in nanocube growth, was taken to be 4 nm.

#### V. SUPPLEMENTARY FIGURES

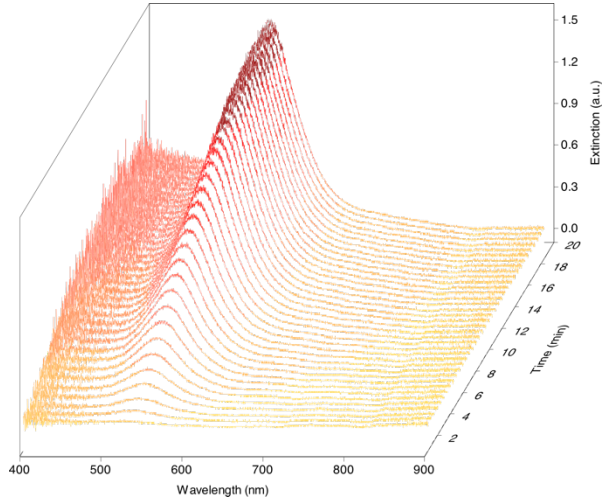


FIG. S1. Time-resolved extinction profile of colloidal Au nanocubes throughout growth.

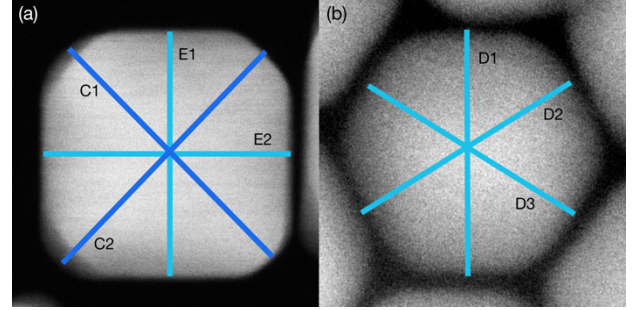


FIG. S2. Schematic representations of NC sizing measurements from STEM images. (a) Cubes were characterized by corner-to-corner (C) and edge-to-edge (E) distances. (b) Cuboctahedra were characterized by side-to-side (D) distances.

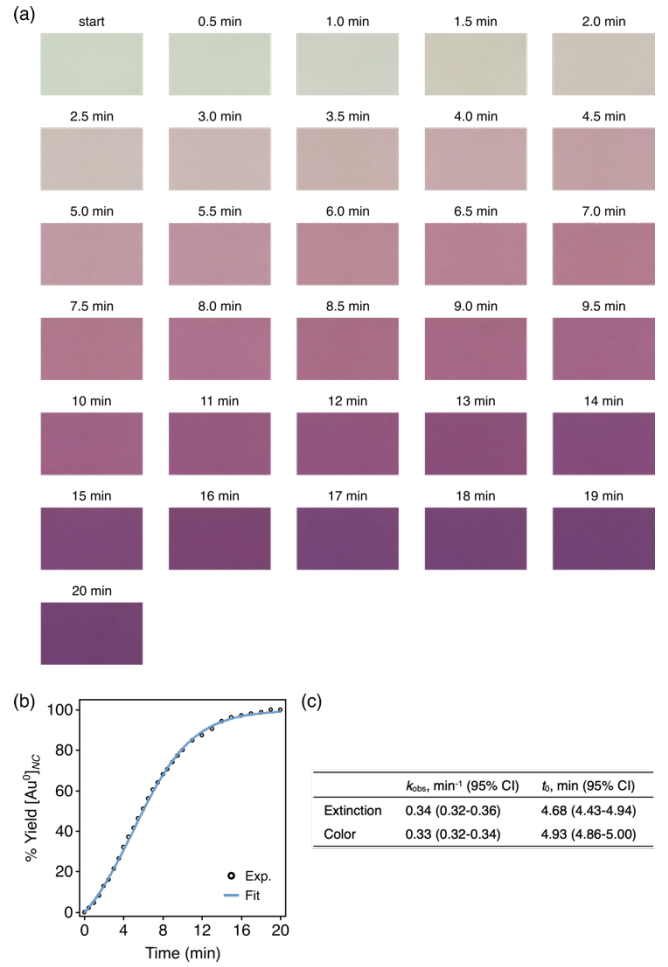


FIG. S3. Kinetics of NC growth analyzed via nanoplasmonic color development. (a) Time-resolved images of nanoplasmonic color throughout the growth of colloidal Au nanocubes. (b) Kinetics of NC growth analyzed via the colors in (a). The data were fitted to Eq. (11) ( $r^2 > 0.99$ ). (c) Comparison of colloidal NC growth kinetics based on extinction and colorimetric images. CI, confidence interval.

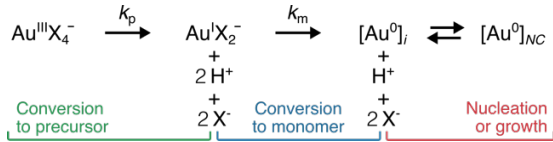


FIG. S4. Reduction pathway of Au during colloidal NC synthesis. X = predominantly Cl<sup>-</sup> with small amounts of Br<sup>-</sup> in our growth formulation. Both reaction mechanisms in Au reduction, disproportionation and direct reduction, result in the same stoichiometry. The addition of H<sup>+</sup> and Cl<sup>-</sup> shifts the dynamic equilibrium, decreasing monomer conversion.

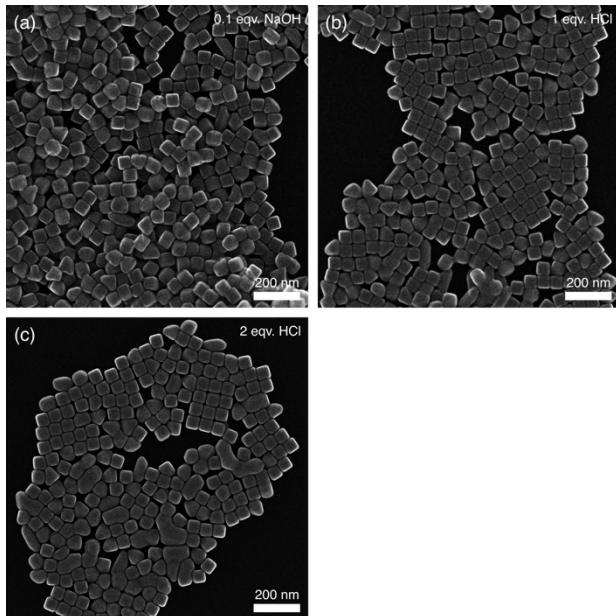


FIG. S5. Large-area SE-STEM images of Au nanocubes after growth. The micrographs show the NCs grown with (a) 0.1 equivalents (equiv.) NaOH, (b) 1 equiv. HCl or (c) 2 equiv. HCl.

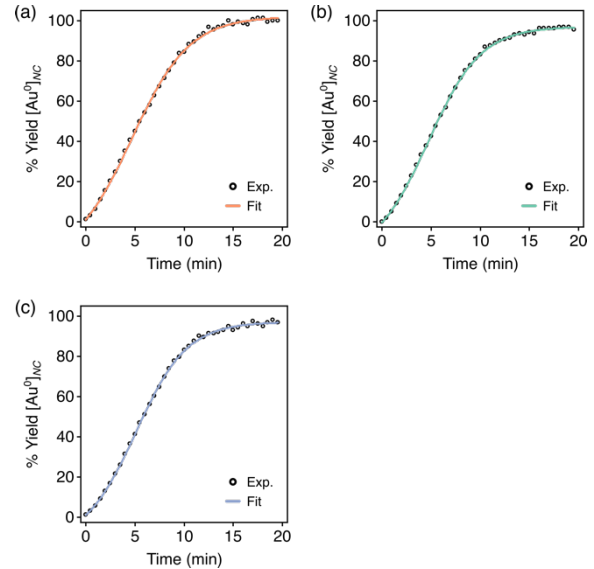


FIG. S6. Kinetics of NC growth analyzed via peak nanoplasmonic extinction. Colloidal Au nanocubes were grown with (a) 0.1 equivalents (equiv.) NaOH, (b) 1 equiv. HCl or (c) 2 equiv. HCl. The data were fitted to Eq. (11) ( $r^2 > 0.99$  for each).

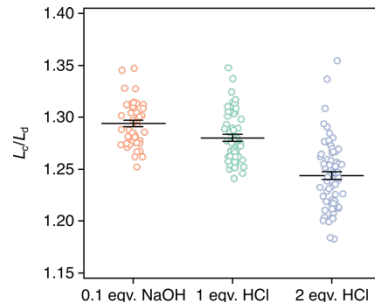


FIG. S7. Comparison of the corner sharpness of nanocubes based on a normalized sharpness index. Measurement parameters are defined in Fig. 4(f). Lines and whiskers represent means and 95% CIs.

## VI. SUPPLEMENTARY TABLES

TABLE S1. Summary of shape evolution throughout colloidal nanocube growth.

	Shape yield (%)					
Time (min)	Cuboctahedra	Truncated cubes	Cubes	Overgrown cubes	Other shapes	Total cubes/ cuboctahedra
<b>0.5</b>	96.3	0.0	0.0	0.0	3.7	96.3
<b>2.0</b>	0.0	77.4	5.3	10.2	7.1	92.9
<b>4.0</b>	0.0	74.0	3.3	15.0	7.7	92.3
<b>7.0</b>	0.0	34.7	35.5	21.9	7.9	92.1
<b>15</b>	0.0	8.6	60.0	24.4	7.0	93.0

TABLE S2. Parameters used to characterize supersaturation and model colloidal NC growth.

Symbol	Definition	Units	Value
$a$	Lattice parameter of Au	Å	4.085
$v_c$	Molar volume of Au	cm <sup>3</sup> mol <sup>-1</sup>	10.3
$C_{\infty}$	Saturation concentration of [Au <sup>0</sup> ] <sub>i</sub>	µM	2.87 [5]
$D$	Bulk diffusion coefficient of monomer/precursor	m <sup>2</sup> s <sup>-1</sup>	9.0 × 10 <sup>-8</sup> [6]
$\nu$	Adatom vibrational frequency	s <sup>-1</sup>	1.0 × 10 <sup>13</sup> [3]
$n_{NC}$	Number of seeds added to growth formulation	-	2.0 × 10 <sup>13</sup>
$d_i$	Size of nanoseeds added to the growth formulation	nm	10.0
$T$	Temperature of growth formulation	K	293.15
$N_A$	Avogadro's number	mol <sup>-1</sup>	6.022 × 10 <sup>23</sup>

TABLE S3. Summary of shape yields for colloidal nanocubes grown with various formulations.

	Shape yield (%)					
Sample	Cuboctahedra	Truncated cubes	Cubes	Overgrown cubes	Tetrahedra	Other shapes
<b>0.1 equiv. NaOH</b>	0.2	32.6	36.8	17.1	7.2	6.2
<b>1 equiv. HCl</b>	0.2	56.7	17.9	7.5	14.7	3.1
<b>2 equiv. HCl</b>	0.4	67.9	2.9	4.0	18.1	6.7

TABLE S4. Summary of kinetics and size for colloidal nanocubes when grown with various formulations.

Sample	$k_{obs}$ , min <sup>-1</sup> (95% CI)	$t_0$ , min (95% CI)	Size, nm (SD)
<b>0.1 equiv. NaOH</b>	0.34 (0.32-0.36)	4.68 (4.43-4.94)	63.9 (0.89)
<b>1 equiv. HCl</b>	0.37 (0.36-0.39)	4.72 (4.58-4.87)	62.8 (1.04)
<b>2 equiv. HCl</b>	0.38 (0.37-0.40)	5.10 (4.95-5.25)	61.2 (1.39)

- 
- [1] J. E. Park, Y. Lee, and J. M. Nam, *Nano Lett.* **18**, 6475 (2018).
  - [2] K. Park, L. F. Drummy, R. C. Wadams, H. Koerner, D. Nepal, L. Fabris, and R. A. Vaia, *Chem. Mater.* **25**, 555 (2013).
  - [3] I. V. Markov, *Crystal growth for beginners: fundamentals of nucleation, crystal growth and epitaxy* 2017), 3rd edition. edn.
  - [4] P. R. Wells, *Chem. Rev.* **63**, 171 (1963).
  - [5] S. A. Morin, M. J. Bierman, J. Tong, and S. Jin, *Science* **328**, 476 (2010).